doi:10.1016/j.ultrasmedbio.2011.10.014

● *Original Contribution*

INTEGRATION OF CRAWLING WAVES IN AN ULTRASOUND IMAGING SYSTEM. PART 2: SIGNAL PROCESSING AND APPLICATIONS

Zaegyoo Hah,* Chris Hazard,[†] Bradley Mills,* Christopher Barry,[‡]
Deborah Rubens,[§] and Kevin Parker*

*University of Rochester, Department of Electrical and Computer Engineering, Rochester, NY; [†] GE Global Research, Niskayuna, NY; [‡] Department of Surgery Division of Solid Organ Transplant and Hepatobiliary Surgery, University of Rochester Medical Center, Rochester, NY; and [§] University of Rochester Medical Center, Department of Imaging Sciences, Rochester, NY

Abstract—This paper introduces methods to generate crawling wave interference patterns from the displacement fields generated from radiation force pushes on a GE Logiq 9 scanner. The same transducer and system provides both the pushing pulses to generate the shear waves and the tracking pulses to measure the displacements. Acoustic power and system limitations result in largely impulsive displacement fields. Measured displacements from pushes on either side of a region-of-interest (ROI) are used to calculate continuously varying interference patterns. This technique is explained along with a brief discussion of the conventional mechanical source-driven crawling waves for comparison. We demonstrate the method on three example cases: a gelatin-based phantom with a cylindrical inclusion, an oil-gelatin phantom and mouse livers. The oil-gelatin phantom and the mouse livers demonstrate not only shear speed estimation, but the frequency dependence of the shear wave speeds. (E-mail: zahah@ece. rochester.edu)   © 2012 World Federation for Ultrasound in Medicine & Biology.

Key Words: Crawling wave, Sonoelasticity, Radiation force, Crawling wave movie synthesis, Local shear speed estimation, Shear speed dispersion.

INTRODUCTION

The fundamental idea behind crawling waves is to use the interference pattern of two shear waves traveling in opposite directions to gain insight into the mechanical properties of tissue. Some of the challenges associated with generating such an interference pattern using radiation force have been reported previously (Hah et al. 2010a, 2010b, 2010c), and in the companion paper, Part 1. This paper will discuss some of the major applications. The technique described here allows exploration of some of the properties of the interference pattern without burdening the system or heating the tissue excessively. The basic idea is to generate the two shear waves separately and record the displacements for each independently. Using these independently gathered displacement datasets, a whole family of crawling wave interference patterns can be synthesized. This assumes that interference between the shear waves is a linear process. For the very small displacements typical of these experiments, the assumption of linearity is valid (Hah et al. 2010b). The idea of linearly superimposing displacements from multiple sources has also been used to improve the illumination and even to allow crude beamforming of the transient shear waveforms in MR (magnetic resonance) elastography (Mariappan et al. 2009).

Crawling waves require two sources that generate shear waves at specific frequencies in the range of 40–1000 Hz. Many earlier crawling wave (CrW) experiments used mechanical continuous wave (CW) excitations that developed characteristic interference patterns. Generating CW shear waves is more difficult with radiation force methods, requiring either repeated pushing pulse excitations or amplitude-modulated CW acoustic excitation (Fatemi and Greenleaf 1998; Konofagou and Hynynen 2003). This can result in tissue heating and a need for more thermal capacity in the pulsing and switching electronics. A more sparing approach is synthetic calculation of crawling waves using short duty-cycle push pulses, which generate impulsive displacement waveforms.

This paper, which complements Part 1, focuses on the theory, methods and applications of CrW synthesis

Address correspondence to: Dr. Zaegyoo Hah, University of Rochester, Department of Electrical and Computer Engineering, Box 270126, Rochester, NY 14627. E-mail: zahah@ece.rochester.edu

from radiation forces to generate acoustic radiation force crawling (ARFC) waves. The methods are verified in phantoms, both homogeneous and inhomogeneous. The frequency selective synthesis of CrW will be applied to extract dispersion characteristics of media including a fatty phantom of and *ex vivo* mouse livers. Comparisons are made between results obtained from mechanical shear wave sources run in sinusoidal steady state, and the synthesized crawling waves from radiation force pushes. Measurements on phantoms and mouse livers are found to be closely comparable.

SIGNAL PROCESSING

Review of crawling waves

A typical CrW setup is shown in Figure 1. Two sinusoidal sources, D apart, vibrate with frequencies ω_0 and $\omega_0 + \Delta\omega$ and amplitudes A_l(left) and A_l(right), respectively. A 1-D medium can be defined by distribution functions for shear speed $c(x)$ and attenuation $\alpha(x)$. We can also define a local wave propagation vector or wave number $k(x) = \omega_0/c(x)$, and shear wave amplitude factor $A(x)$ to account for the decrease of the amplitude of the waves in the stiffer region (Gao et al. 1995). For simplicity, $A(x)$ is considered to be a correlated parameter. Therefore, the CW signal coming from the left $L(x,t)$ and the right $R(x,t)$ source can be written as

$$L(x,t) = A_l A(x) e^{-\int_0^x \alpha(x)dx} e^{-j\int_0^x k(x)dx} e^{-j\omega_0 t}, \text{ and}$$
$$R(x,t) = A_r A(x) e^{\int_D^x \alpha(x)dx} e^{-j\int_D^x k(x)dx} e^{-j\Delta\omega t} e^{j\phi_0} e^{-j\omega_0 t}, \tag{1}$$

where ϕ_0 is the difference in the initial phase between the sources that generate the $L(x,t)$ and $R(x,t)$ waves.

Our main objective is to recover the shear speed distribution of $c(x)$ or $k(x)$ and possibly $\alpha(x)$ and $A(x)$ as well, in eqn (1). Because both of the sources are vibrating simultaneously, the observed signal is given by $O(x,t) = L(x,t) + R(x,t)$, a sum of harmonic signals. To extract the magnitude of the shear waves, the square of the amplitude (or variance) of the observed signal is calculated as
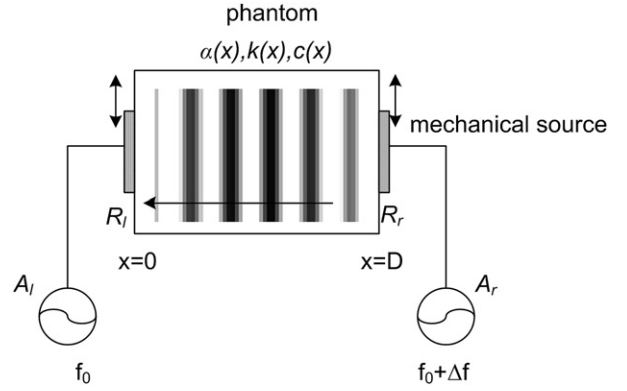

Fig. 1. A diagram showing the basic configuration for CrW. Two sources with frequency of f and $f + \Delta f$ and amplitude of A_l, A_r are vibrating continuously. The medium can be defined with distribution function of shear speed $c(x)$, attenuation $\alpha(x)$, wave number $k(x)$ and reflection coefficients R_l and R_r at the left and right boundaries, respectively.

describes the moving interference pattern. For small difference frequencies, $\Delta\omega \ll 2\pi$, the pattern moves slowly, which allows tracking at low frame rate. For example, for $\Delta f = 0.2$ Hz, a frame rate of 5 Hz will generate 25 frames for each period of CrW. The baseline term, containing the $\alpha(x)$ component, is steady and can be fitted into the formula to estimate the attenuation of the medium. The crawling wave term, including $k(x)$, is the term that moves slowly, because of $\Delta\omega t$ term, and will provide the information of the shear wave speed or the stiffness of the medium. These output parameters are generally a function of the frequency. Changing the driving frequency and subsequent estimation will provide the dispersion characteristics of the medium.

Extracting the shear speed from the CrW term of eqn (2) can take many forms. For simplicity, we will explain phase-based estimation. Filtering and other methods can be used on the CrW term to recover the phase, $\theta(x)$, of the cosine term in eqn (2), from the measured displacement field as

$$|O(x,t)|^2 = (L+R) \cdot (L+R)*$$
$$= A_l^2 A(x)^2 e^{-2\int_0^x \alpha(x)dx} + A_r^2 A(x)^2 e^{2\int_D^x \alpha(x)dx} +$$
$$2A_l A_r A(x)^2 e^{-\int_0^D \alpha(x)dx} \cdot \cos\left[\Delta\omega t + 2\int_0^x k(x)dx - \int_0^D k(x)dx + \phi_0\right] \tag{2}$$
$$= \text{baseline} + \text{time dependent moving pattern.}$$

As seen in eqn (2), this CrW signal has a baseline term that depends on the attenuation and amplitude distribution, and a time-dependent sinusoidal term that

$$\theta(x) = 2\int_0^x k(x)dx + \text{constant.} \tag{3}$$

The wave number, $k(x)$ and the shear velocity, $c(x)$, can then be calculated by taking a numerical derivative as

$$k(x) = \frac{\theta'(x)}{2}, and$$
$$c(x, \omega_0) = \frac{2\omega_0}{\theta'(x)}. \qquad (4)$$

Estimation the phase $\theta(x)$ can be done pixel by pixel through a slow-time filter (Castaneda et al. 2007) using the knowledge of $\Delta\omega$, or frame by frame though Hilbert transform (Hoyt et al. 2008). In reality, the CrW data is often contaminated by noise and therefore some degree of smoothing is required to make $\theta'(x)$ smooth and well-behaved. There are many reports of methods used to extract shear speeds from CrW experiments on phantoms and *ex vivo* and *in vivo specimens*, including a local spatial frequency estimator, estimation of pattern arrival times, and local autocorrelation (McLaughlin and Renzi 2006; McLaughlin et al. 2007; Wu et al. 2006; Hoyt et al. 2008; Castaneda et al. 2007; Hoyt et al. 2007, 2006; Castaneda et al. 2009).

There are factors to consider when performing experiments in phantoms and specimens. First, the amplitudes of the driving signal A_l, A_r should be comparable to avoid one source dominating the field. Second, the boundary should be properly modified to minimize reflections, denoted in Figure 1 as R_l and R_r, for the boundary reflection at left and right source, respectively. Figure 2 shows results from a simulation with a 1-cm inclusion with peak shear speed of 5 m/s in a background medium of 3 m/s of speed and 1 dB/cm of attenuation. Both the inclusion and the background medium are assumed to have the same density of 1 g/cm³. The shear speed distribution and shear wave amplitude profile, given from source amplitude, attenuation and amplitude factor, are shown in Figure 2a and 2b, respectively. Some frames of the CrW movies, with and without boundary reflections, are shown in Figure 2c and Figure 2d, respectively. As seen in Figure 2d, calculated with $R_l = R_r = 0.5$, reflections cause amplitude variation "pulsating" with a regular pattern. The effect of reflections on the phase and the speed estimation are illustrated in Figure 2 (e, f). The phase of the homogeneous phantom is unwrapped and shown in the solid line for no reflection and in the dotted line with boundary reflection, respectively, in Figure 2e. The slope of the curve is inversely proportional to the shear speed as formulated in eqn (4). Indeed, the slope is smaller near the inclusion. With reflections, however, the phase, $\theta(x)$, shows a sinusoidal fluctuation as the dotted line of Figure 2e shows. Thus, the shear speed estimation, $c(x)$, would vary similarly as shown in Figure 2f. A detailed description of the reflection effect on CrW is beyond the scope of this paper.

Reflection removal

Shear waves generated with radiation force can exhibit reflections that can corrupt the shear speed estimation algorithms. Because the shear waves in this study are impulsive, the reflections can be removed with a motion filter. Figure 3a illustrates an example of an impurity inside an oil-gelatin phantom that generated a reflection. The displacement data is acquired with the parameters explained in the part 1 paper with a ROI of 4 cm deep and 18 mm wide. Figure 3b is an image of the displacements at a fixed depth, indicated as line *A* in Figure 3a, as a function of time *vs.* the lateral location. The reflection is clearly seen in Figure 3 (a, b). A filter or mask based on the peak Radon Transform (Rouze et al. 2010) of the data can be applied to track the motion of the main shear wave as shown in Figure 3 (c–e). Each of the points inside the peak region of the Radon transformation shown in Figure 3d will construct a line in the original image of Figure 3b, and collecting all those lines and smoothing will produce a motion mask shown in Figure 3e. Although the motion mask shown in Figure 3e is a simple 2-D filter, a 3-D filter is actually constructed by combining all of the 2-D filters at each depth and smoothing them. Figure 3f shows the motion-filtered image of Figure 3b with estimated shear speed of 2.9 m/s. As explained in Figure 2, the reflection causes distortion of the phase and resultant shear speed estimation, as illustrated in Figure 3g and Figure 3h, with and without the motion filter, respectively. The detailed procedure of calculating the phase from the synthesis will be discussed in the next section. This approach removes the reflected components of shear waves because their displacements do not follow the time history of the forward propagating shear wave. If the reflections are not removed, the shear speeds estimated from the synthesized patterns can be affected.

Synthesis of crawling waves from displacements generated from radiation force

With the displacement data filtered to remove ambient noise, vibrations and reflections, the left and right datasets can be used to generate ARFC wave sequences (Hah et al. 2010a, 2010c). It should be noted that the ARC synthesis schemes presented here are aimed at producing CrW that can be closely compared with mechanically driven, continuous wave CrW. For that reason, we focus on direct synthesis methods in this section in preference over the FFT. Moreover, the inherent assumption of periodicity of FFT can modify the estimation results.

The delay-add method, graphically depicted in Figure 4, illustrates an intuitively straightforward procedure to synthesize the continuous waveform, which is also simple to implement. Let the displacement from
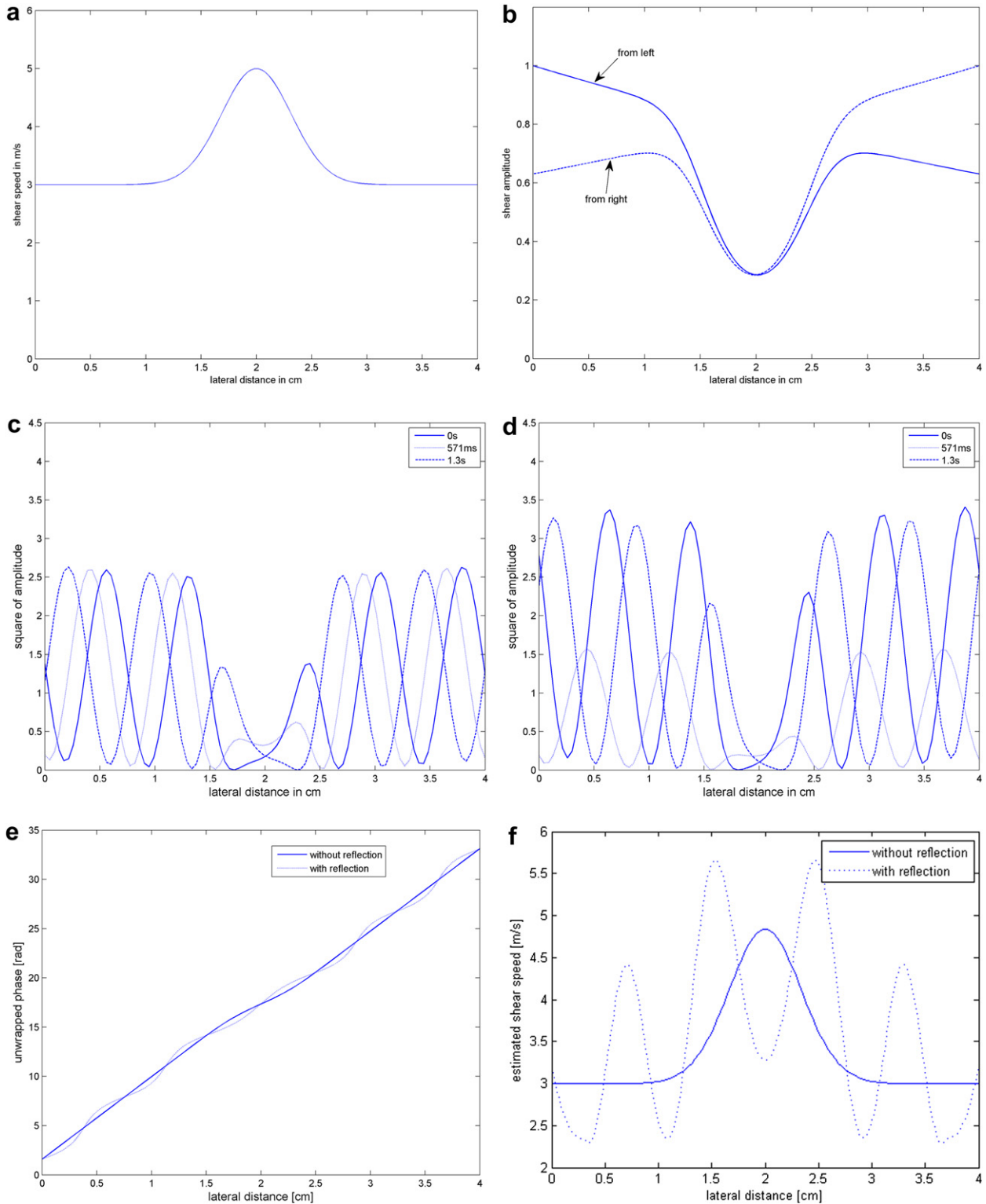
Fig. 2. A simulation result showing the behavior of CrW. (a) Shear speed distribution with a 1-cm inclusion inside a background medium of 3 m/s. (b) Amplitude distribution of the left and right signals without boundary reflection as a product of source magnitude, attenuation and amplitude factor. (c) Displays the CrW movement without reflection and (d) shows the same movement with boundary reflection of 0.5 at both sides, causing the amplitude variation to pulsate in a regular pattern. The unwrapped phase distribution is shown in (e), where it is clear that the phase for (d) is corrupted with a sinusoidal component. The estimated shear speed for phase distribution of (e) is shown in (f).
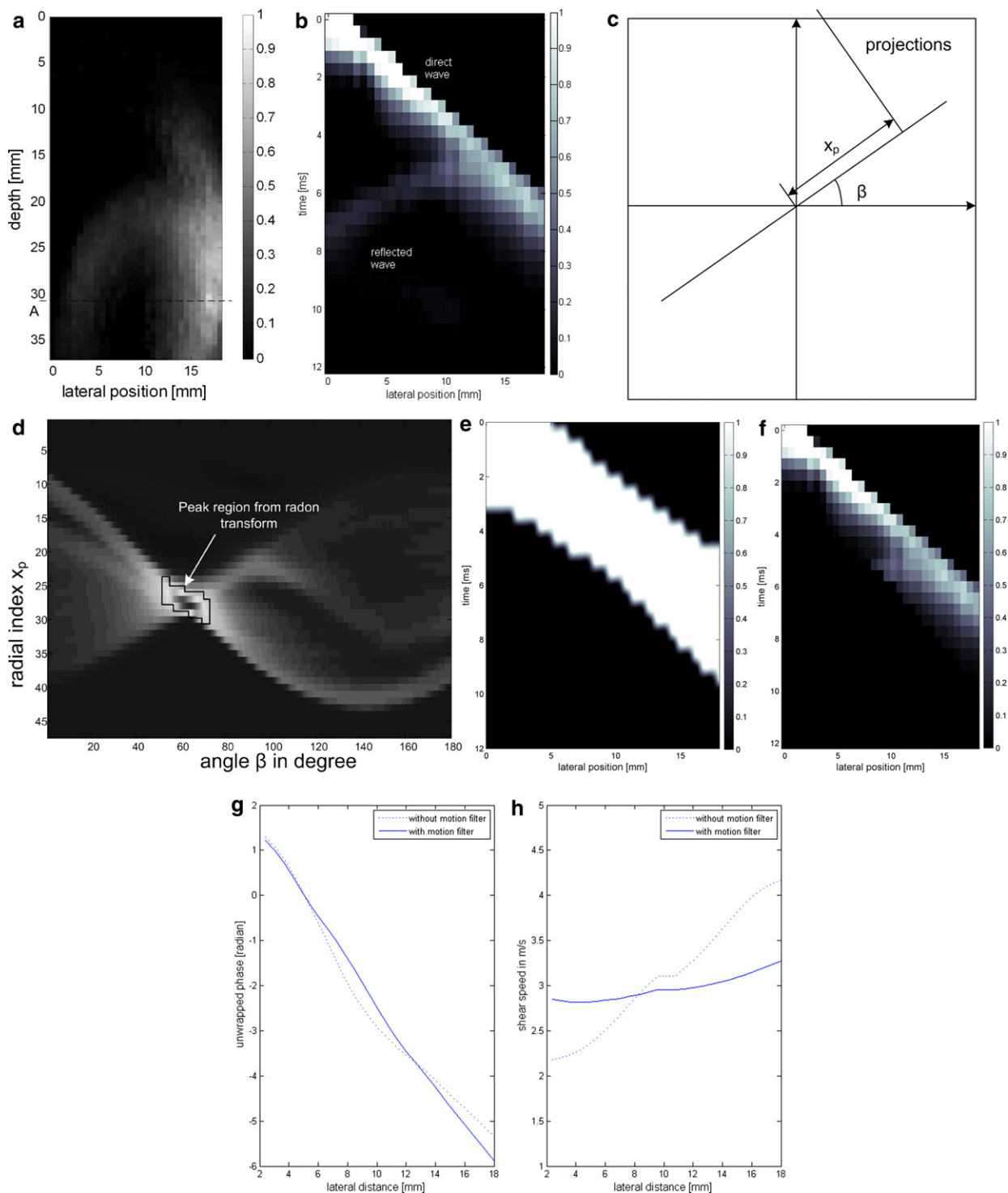
Fig. 3. An example of shear wave displacements from radiation force with reflection. (a) A frame of the shear wave displacements shows a reflected wave. An image slice at depth *A* of (a) is shown in (b), where the direct wave is clearly discernible from the reflected wave. (c) The concept of radon transformation with angle β and radial distance x_p. (d) The result of radon transform. The peak region is marked. Each of the points inside the peak region converts to a single line in the original image. Combining these lines and smoothing produces a final motion mask shown in (e). (f) Motion-filtered image. The phase distribution and the estimated shear speed are shown in (g) and (h), respectively, with and without motion filtering.
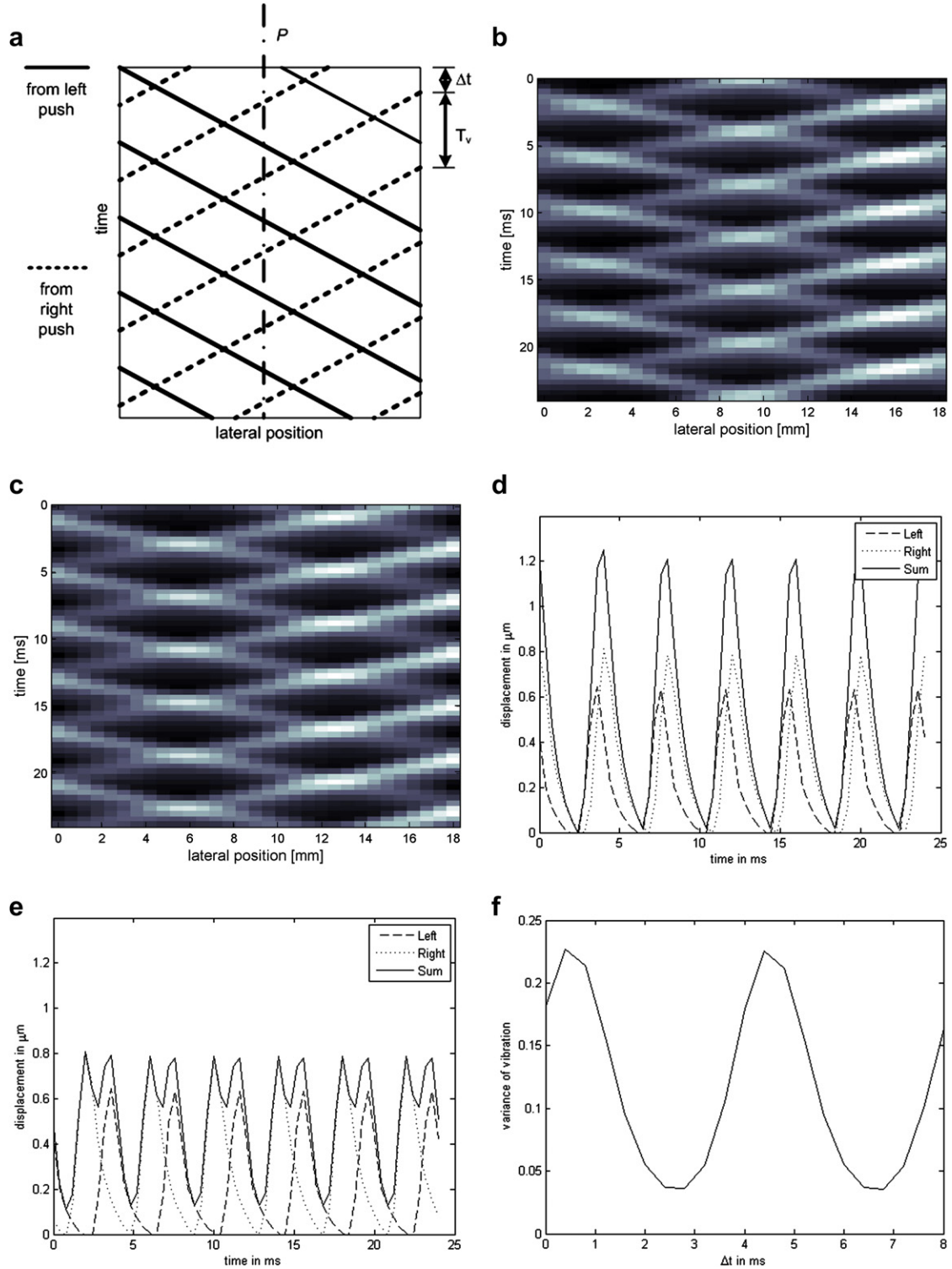
Fig. 4. (a) Concept of delay-add where the waveform from the left and the right push are repeated with the rate of $f_v = 1/T_v$. Δt is the time shift of the one side firing relative to the other side firing. (b) A slice image of motion with $f_v = 250$ Hz, $\Delta t = 0$ms. (c) A slice image of motion with $f_v = 250$ Hz, $\Delta t = 2$ ms. (d) Displacements at the depth of 25 mm, 9 mm from the left edge with $f_v = 250$ Hz, $\Delta t = 0$ms for the left push, the right push and the sum of the left and the right, respectively. (e) Displacements at the depth of 25 mm, 9 mm from the left edge with $f_v = 250$ Hz, $\Delta t = 2$ ms for the left push, the right push and the sum of the left and the right, respectively. (f) Derived interference pattern from variance as a function of the slow time at the depth of 25 mm, and 9 mm from the left edge.

the left push be given by $L(x, t)$ at position x and time t. The displacement field that would occur if the system had transmitted a series of push pulses can be calculated by convolving the displacements for a single push with a train of discrete impulses spaced at $T_v = 1/f_v$. The resulting delay-added version $L_{da}(x, t)$, is given by

$$L_{da}(x, t) = \sum_n L(x, t - nT_v), \qquad (5)$$

There is an initial transient portion of the displacement field during which the residual displacements from the previous pushes are building, but eventually the system reaches a steady state and the displacements oscillate over the period T_v. A single period of the steady state L_{das} of the $L_{da}(x, t)$ can be isolated by

$$L_{das}(x, t) = L_{da}(x, t) \cdot \Pi(t/T_v - M), \text{ where}$$
$$\Pi(\tau) = 1, \quad -1/2 < \tau < 1/2. \qquad (6)$$
$$= 0, \quad \text{otherwise}$$

The parameter M in eqn (6) is chosen such that $L_{da}(x, t)$ has reached the steady state. The same can be done for the right-side push. Let Δt be the difference in time between simulated pushes on the left and right sides. Then the $CrW(x, \Delta t)$ are synthesized as

$$CrW(x, \Delta t) = \text{var}[L_{das}(x, t) + R_{das}(x, t)]$$
$$= \text{var}\left[\sum_n (L(x, t - nT_v) + R(x, t - \Delta t - nT_v)) \cdot \Pi(t/T_v - M)\right], \qquad (7)$$

where *var* indicates taking the variance of the signal over one period. By varying the time, Δt, between left and right pulse trains, a series of CrW frames can be synthesized and the shear velocity can be extracted from that data. Figure 4a is a pictorial representation of this interference phenomenon. The solid lines represent the wavefronts of the shear displacement created by the left push, traveling through the ROI from the left to right. The dotted lines represent the waves traveling from right to left and generated by the push on the right side of the ROI. The multiple lines correspond to the synthetically created multiple pushes, with T_v seconds between the simulated pushes. The point of intersection between the solid and dotted lines represents the points of maximum constructive interference between the two waves. The delay between the left and right waveforms, Δt, is also illustrated in Figure 4 (a–c) and shows the resulting displacement images for two particular Δt values: 0 ms and 2 ms, respectively. The depth at which these displacements are calculated is 25 mm and $T_v = 4$ ms ($f_v = 250$ Hz). Figure 4 (d, e) shows profiles from the center of the ROI for the same two values of Δt. The waves from each side and the sum of the waves are shown in the figures. For each spatial point, the sum of the left and the right signal changes as a function of Δt. Calculating

the variance of the sum, over one period, as a function of Δt provides a type of CrW interference pattern as shown for one spatial location in Figure 4f. A curve similar to that shown in Figure 4f can be created for each spatial location. The variance at each location for a given value of Δt can be displayed as an image, and a stack of these images for varying values of Δt can be shown as a movie. In such a movie, the interference pattern can be seen to move or "crawl" across the ROI. Figure 5 demonstrates the ability to create ARC waves using the displacement data. Figure 5 (a–c) shows frames of a crawling wave interference movie for three different values of Δt and for $T_v = 2$ ms ($f_v = 500$ Hz). The "fingers" of the interference pattern can be seen to move through the ROI. Figure 5 (d, e) shows interference patterns for a single value of Δt for lower frequencies, $f_v = 125$ Hz and 250 Hz respectively. The interference movies can be further analyzed with a group of local shear speed estimators.

Although the delay-add method provides a synthesized CrW movie, the movie contains the harmonic components of the fundamental frequency at which the movie was synthesized. Filtering around the frequency band of interest can allow one to extract the parameters for that frequency. However, an alternative method of

synthesis would be a more direct way to achieve the filtering: convolution with a sinusoid. This method assumes that the displacement obtained from the left and the right push has sufficient energy in the frequency band of interest. For the impulsive excitations used in the experiments described here, the duration of the push is very small relative to the period, T_v, of the synthesis. For a reasonable choice of frequencies, there will be an ample signal and the displacements measured approximate an impulse response. The steady state response at f_v caused by the left and the right push would then be

$$L_{con}(x, t) = [L(x, t) * \sin(\omega_v t)] \cdot \Pi(t/T_v - M),$$
$$R_{con}(x, t) = [R(x, t) * \sin(\omega_v t)] \cdot \Pi(t/T_v - M). \qquad (8)$$

The convolution of the impulse response with the sine wave can be viewed as a filter in the frequency domain. In the frequency domain, the sine wave's transform is a delta function at the frequency of the sine wave, which is multiplied by the frequency response of the shear wave. Because the length is truncated, there is broadening of the frequencies extracted by the convolution with a sinc function. However, the harmonic components present in the standard delay-add method
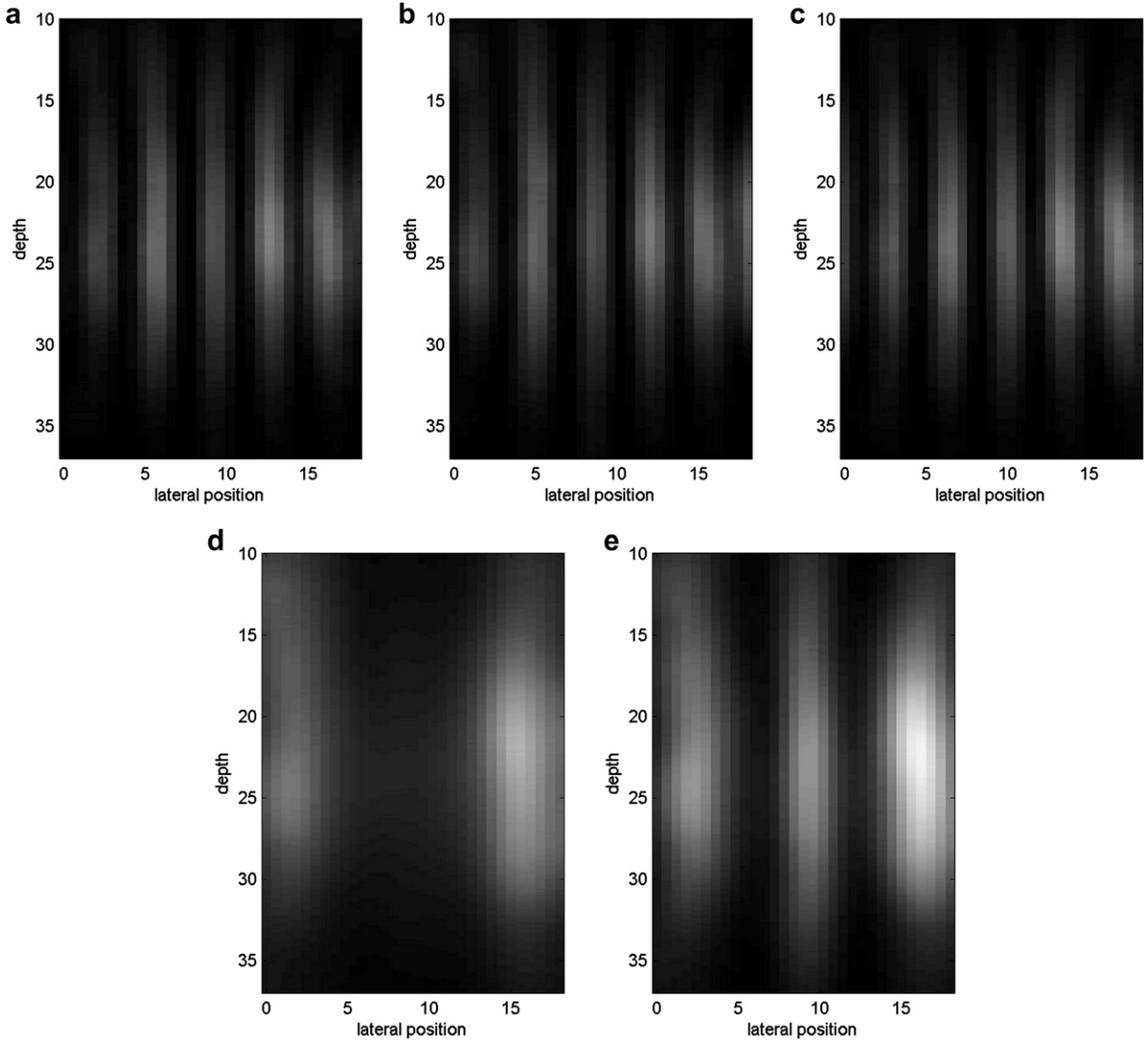
Fig. 5. Derived interference patterns of the left and the right push using the delay-add method. (a–c) Movement of the interference pattern at $f_v = 500$ Hz. (d, e) Interference pattern at $f_v = 125$ Hz and 250 Hz, respectively.

would be suppressed. The crawling wave would then be generated as

$$CrW(x, \Delta t) = var[L_{con}(x,t) + R_{con}(x, t - \Delta t)]. \quad (9)$$

Figure 6 illustrates the procedure of the sine wave convolution-based synthesis method. The displacement from the left push, shown in Figure 6a, is convolved with a sinusoidal tone burst (Fig. 6b) of frequency $f_v = 150$ Hz, resulting in Figure 6c. One period of the steady state is shown in Figure 6d for both the left and right push. By varying the time between the left and right pushes, Δt, the variance as a function of this delay can be calculated over an entire period, as shown in Figure 6e. Using this method at multiple frequencies

allows one to determine the dispersion and ultimately to fit to models of the shear speed, shear modulus and viscosity parameters.

Experimental materials

Three experiments are described. In each of the experiments, displacement data were collected from the left and right radiation force push. The axicon focus described in the companion paper (Part 1) was selected to lower the peak intensity while creating a longer axial source, as compared with conventional focus. The displacement data were used to create CrW movies by using the convolution method, and the CrW movie was analyzed to extract the shear wave speed for the vibration
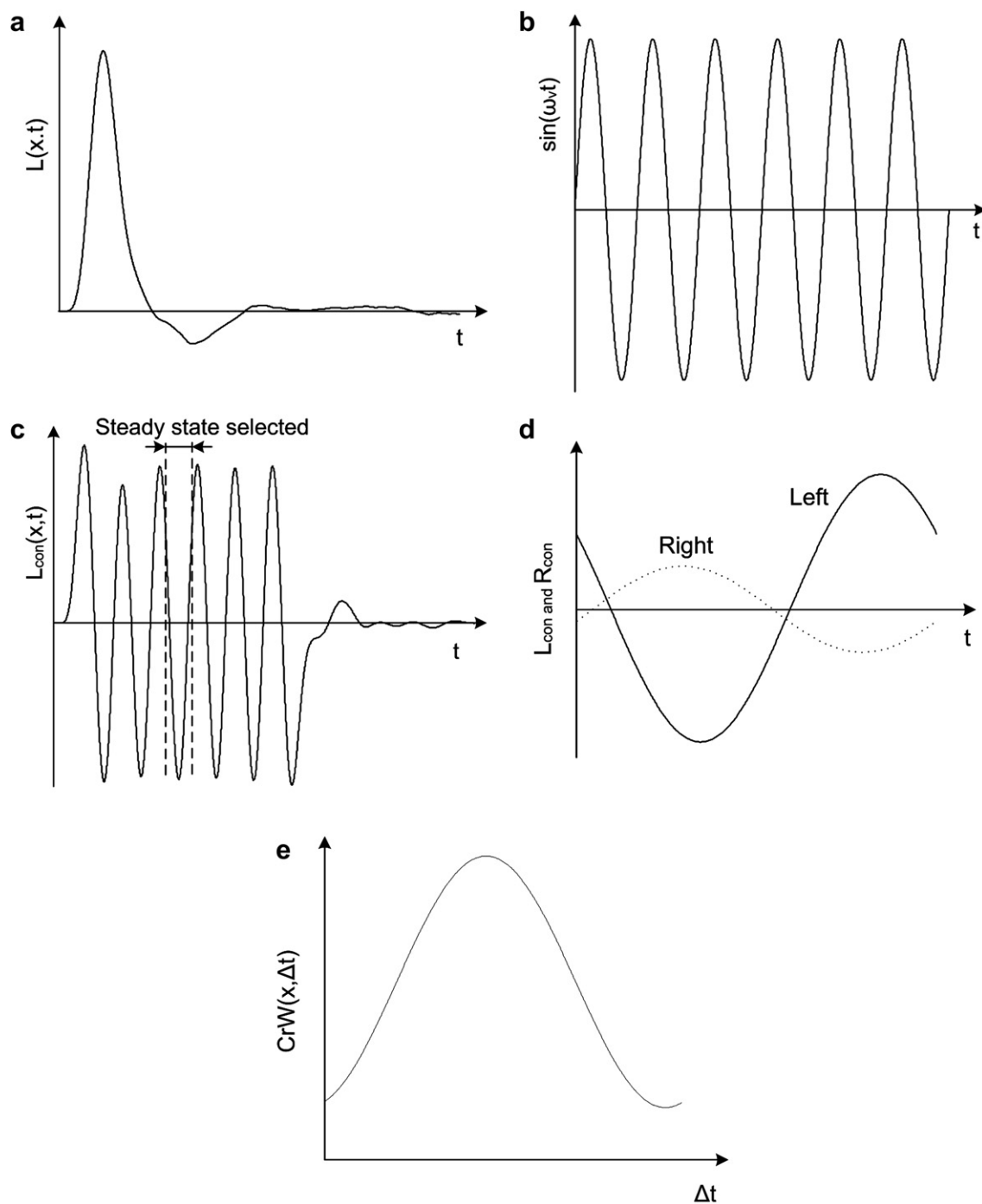
Fig. 6. Procedure of CrW synthesis based on convolution. A displacement recorded from the left push (a) is convolved with a sinusoid (b) to synthesize the CrW movie to produce the waveform shown in (c). Selecting a period of the steady state produces L_{con} and R_{con} shown in (d). By shifting one relative to the other, a complete cycle is generated as shown in (e).

frequency. The constructed phantoms include a gelatin phantom with a cylindrical inclusion, an oil-gelatin phantom and two mouse livers *ex vivo*.

A gelatin phantom (an "inclusion" phantom) with a cylindrical inclusion was fabricated with an inclusion, 6 mm in diameter, of 16% gelatin against a background

of 8% gelatin. The procedure to fabricate the phantom is as follows: 51.5 g gelatin (300 Bloom Pork Gelatin, Gelatin Innovations Inc., Schiller Park, IL, USA), 4.5 g NaCl and 0.75 g of agar were added to 500 mL of deionized water and the mixture was heated to 55°C. After all the components dissolved, the mixture was further
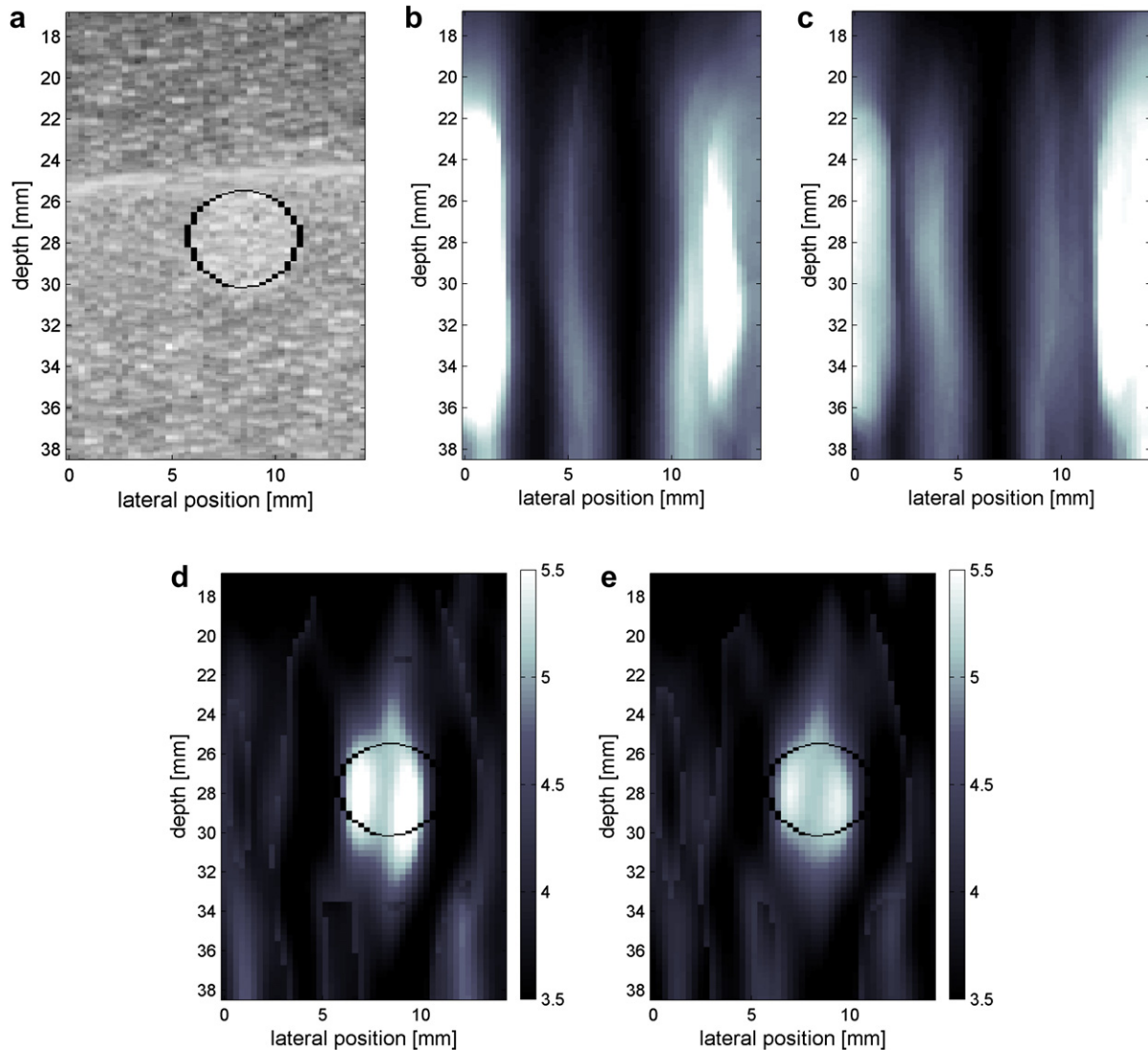
Fig. 7. A B-mode image of the phantom with a 6-mm inclusion is shown in (a) with an outline of the inclusion. Two frames of the CrW movie synthesized at 250 Hz and 300 Hz are shown in (b) and (c), respectively. Grayscale is relative variance of displacement over time. The estimated shear speed images are shown in (d) and (e) for the frequency of synthesis at 250 Hz (d), and 300 Hz (e), respectively.

cooled to approximately 30°C and poured into cylindrical molds and allowed to rest at 4°C overnight. Once formed, the inclusion was removed from the mold and suspended in a cubic phantom mold. An 8% gelatin background was created by heating a mixture of 1.8 L de-ionized water, 148.3 g gelatin, 16.2 g NaCl and 2.7 g agar to 55°C. The mixture was then cooled in an ice water bath to approximately 30°C and poured into the cubic gelatin mold containing the cylindrical inclusion. The mold was then allowed to rest at 4°C overnight. The 8% gelatin background was also used to suspend the mouse livers, as will be discussed in the next section.

Another phantom, an oil-based gelatin phantom, was created to check the dispersion. It consisted of 11% gelatin and 25% castor oil. One-hundred-ten grams

gelatin (300 Bloom Pork Gelatin, Gelatin Innovations Inc.) and 1 g antibacterium (Germall Plus, Lotioncrafter, Olga, WA, USA) were added to 1 L of deionized water, and the mixture was heated to 90°C (molten gelatin). The molten gelatin was placed in an ice water bath and cooled to roughly 55°C at which point 30 mL castor oil and 7.7 mL surfactant (Ultra Ivory, Procter & Gamble, Cincinnati, OH, USA) were emulsified into the mixture. The mixture was further cooled to approximately 30°C, poured in a cubic mold and allowed to rest at 4°C overnight.

A third phantom—mouse phantom—is a gelatin phantom containing mouse livers. The livers, obtained by hepatectomy, were suspended in a cube-shaped mold of 8.5 × 10 × 19 dimension. Two mouse livers were
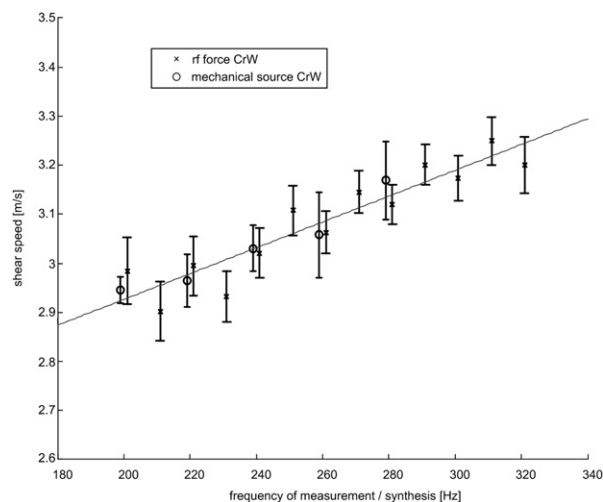
Fig. 8. Dispersion measurement for the oil-gelatin phantom. The phantom consists of 11% gelatin and 30% castor oil. Because of the viscosity provided by the oil, the phantom is expected to have significant dispersion as this result verifies. The results from the CrW with mechanical vibrators and the synthesized CrW from radiation force pushes are shown. The error bars indicate the standard deviation of the processed region of interest. The dispersion shows the slope of 0.26 m/s per 100 Hz.
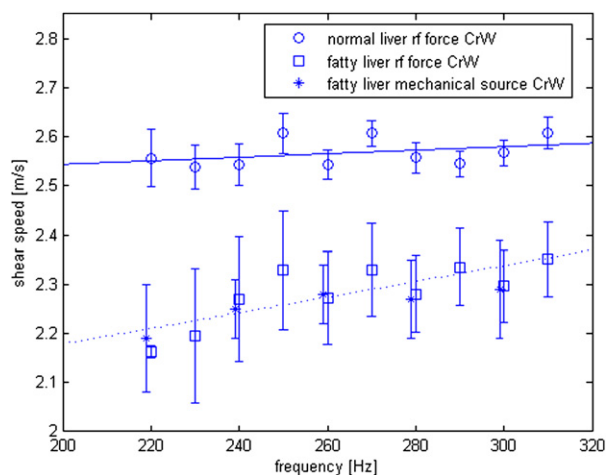

Fig. 9. Shear speeds estimated from the synthesized crawling wave movies at different frequencies. Two mouse livers—one normal and one fatty—were chosen. The normal mouse liver shows higher shear speed than the fatty mouse liver. The fatty mouse liver shows larger dispersion.

suspended in the mold and the 8% gelatin phantom previously described was poured into the cubed gelatin mold containing the mouse livers. The mold was then placed in an ice water bath for roughly 90 min, cooling it from 35°C to 15°C. The size of the liver in the scanning cross-section was approximately 2 $\times$ 3 cm for the fatty liver, and 1.5 $\times$ 1.4 cm for the normal liver.

RESULTS AND DISCUSSIONS

Crawling waves synthesized from the displacement fields generated from the short push on the left and the right side were used to estimate the elastic properties of each medium. Data were acquired with the setup and parameters explained in part 1 of this paper, ROI of 4-cm depth and 18-mm width, a push tone burst of 5 MHz 250 μs long, pulse repetition frequency of 2.5 kHz and 48 tracking vectors firings in the packet.

Figure 7 shows a B-mode image of the inclusion phantom, two sample images of the synthesized ARC wave movies at 250 Hz and 300, Hz respectively, using eqn (9) and shear speed estimation results at the two frequencies of CrW synthesis. The shear speed estimation results of Figure 7(d, e) are shown with the outline of the inclusion. The estimated shear speed was approximately 3.5 m/s for the 8% background and 5.4 m/s for the inclusion. It should be noted that shear speed is sensitive to temperature of the phantom: the lower the temperature the higher the estimated speed. The data in Figure 7 were obtained at about 16°C, lower than room tempera-

ture. That is why the estimated speed is a little higher than the previous estimation of similar phantoms by Hoyt et al. (2008). The resolution increases with the synthesis frequency, as can be seen comparing Figure 7(d,e). Because the propagation direction of CrW is horizontal, the horizontal resolution is better than the vertical resolution.

It is known that the shear wave speed of a viscoelastic medium is a function of frequency (Chen et al. 2009; Deffieux et al. 2009; Oestreicher 1951; Blackstock 2000). The oil-gelatin phantom described in the previous section was scanned both with mechanical vibrators at different frequencies ranging from 200–280 Hz and with radiation force pushes, from which CrW were synthesized for frequencies from 200–320 Hz according to eqn (9). The results are shown in Figure 8. Because of the viscosity provided by the oil, the phantom should exhibit dispersion and this is seen in the resulting data. Both the results from the mechanical and the synthesized crawling waves show a good match, both displaying change of shear speed with frequency. The dispersion shown in Figure 8 was calculated to have the slope of 0.26 m/s per 100 Hz. This example demonstrates the additional use of crawling waves to assess dispersion over a range of accessible shear wave frequencies.

This approach was further applied to two mouse livers *ex vivo*: one normal and one fatty. A leptin-deficient mouse is a well-characterized model of morbid obesity and type 2 diabetes and is marked with hepatic steatosis (Pelleymounter et al. 1995). The mice were purchased (Jackson Laboratories, Bar Harbor, ME, USA) and housed in a vivarium (University of Rochester,

Rochester, NY, USA) for at least one week before they were sacrificed [All animal protocols are approved by the University of Rochester Committee on Animal Resources (IACUC Approval Date 1/4/2010, Animal Welfare Assurance Number A329201)].

The livers were embedded in gelatin and were scanned using both mechanical vibration sources and radiation force pushes. The shear wave speed estimation results are shown in Figure 9 for frequencies from 220–310 Hz. The shear speed of the normal mouse liver (shown as a circle in Fig. 9) shows a mean speed of about 2.55 m/s. On the other hand, shear speed for the fatty liver (shown as a square for radiation force CrW and as a star for mechanical source CrW, respectively) is lower, in the range of 2.2–2.37 m/s. It is hypothesized that the increased fat content of mouse liver gives rise to higher viscosity, which contributes to the dispersion of shear speed, as was also shown for the oil-gelatin phantom shown in Figure 8. Different viscoelastic models could be fit to the data; however, a larger frequency band would be required to have high confidence in the parameter fit (Sridhar and Insana 2007; Sridhar et al. 2007; Caputo 1967).

The results from synthetic crawling waves are found to be closely comparable with those derived from the use of mechanical shear wave sources, in phantoms and mouse livers. This suggests that either method (radiation force push or mechanical shear wave sources) can be used to create crawling waves. However, in phantoms, the use of mechanical crawling waves produces a larger displacement (higher signal-to-noise reduction) over a larger ROI, and without any significant heating concerns.

CONCLUSION

Crawling waves can be created from radiation force pulses on the right and left sides of a ROI that generate opposing shear waves. The shear waves can be created by a long series of pulses on each side, or equivalently they can be calculated from the response to a single pulse from each of the right and left sides of the ROI. The calculated crawling waves can be derived for a set of frequencies within the bandwidth of the original propagating shear waves.

This has the advantage of separating out the phase velocities at discrete frequencies, and leads to a measurement of the dispersion, or change in velocity over frequency. The dispersion in tissues is related to the lossy or viscoelastic behavior of tissues and is therefore a potentially valuable parameter to assess. The crawling waves produced by this integrated system are also capable of resolving small inhomogeneities on the order of 3 mm in radius.

REFERENCES

Blackstock D. Fundamentals of physical acoustics. New York: John Wiley & Sons, 2000.

Caputo M. Linear models of dissipation whose q is almost frequency independent-II. Geophys J R Astr Soc 1967;13:529–539.

Castaneda B, An L, Wu S, Baxter L, Yao J, Joseph J, Hoyt K, Strang J, Rubens D, Parker K. Prostate cancer detection using crawling wave sonoelastography. Proc SPIE 2009;7265:726513-1–726513-10.

Castaneda B, Hoyt K, Zhang M, Pasternack D, Baxter L, Nigwekar P, Sant'Agnese A, Joseph J, Strang J, Robens D, Parker K. Prostate cancer detection based on three dimensional sonoelastography. Proc IEEE Ultrason Symp 2007;1353–1356.

Chen S, Urban M, Pislaru C, Kinnick R, Zheng Y, Yao A, Greenleaf J. Shearwave dispersion ultrasound vibrometry (SDUV) for measuring tissue elasticity and viscosity. IEEE Trans. Ultrason Ferroelectr Freq Control 2009;56:55–62.

Deffieux T, Montaldo G, Tanter M, Fink M. Shear wave spectroscopy for in vivo quantification of human soft tissues viscoelasticity. IEEE Trans Med Imaging 2009;28:313–322.

Fatemi M, Greenleaf J. Ultrasound-stimulated vibro-acoustic spectrography. Science 1998;280:82–85.

Gao L, Parker K, Alam S, Lerner R. Sonoelasticity imaging: Therory and experimental verification. J Acoust Soc Am 1995;97:3875–3886.

Hah Z, Cho Y, An L, Hazard C, Rubens D, Parker K. Methods for generating crawling waves with radiation force from ultrasonic beams. J Ultrasound Med 2010a;29:S60.

Hah Z, Hazard C, Cho Y, Rubens D, Parker K. Crawling waves from radiation force excitation. Ultrasonic Imaging 2010b;32:177–189.

Hah Z, Hazard C, Rubens D, Parker K. Synthesis and analysis of crawling waves generated from radiation force. Proceedings of the Ninth International Conference on the Ultrasonic Measurement and Imaging of Tissue Elasticity 2010c;058:119.

Hoyt K, Castaneda B, Parker K. Two-dimensional sonoelastographic shear velocity imaging. Ultrasound Med Biol 2008;34:276–288.

Hoyt K, Parker K, Rubens D. Sonoelastographic shear velocity imaging: experiments on tissue phantom and prostate. Proc IEEE Ultrasonics Symp 2006;1686–1689.

Hoyt K, Parker K, Rubens D. Real-time shear velocity imaging using sonoelastographic techniques. Ultrasound Med Biol 2007;33:1086–1097.

Konofagou E, Hynynen K. Localized harmonic motion imaging: theory, simulations and experiments. Ultra sound Med Biol 2003;29:1405–1413.

Mariappan Y, Rossman P, Glaser K, Manduca A, Ehman R. Magnetic resonance elastography with a phased-array acoustic driver system. Magn Reson Med 2009;61:678–685.

McLaughlin J, Parker K, Renzi D, Wu Z. Shear wave speed recovery using interference patterns obtained in sonoelastography experiments. J Acoust Soc Am 2007;121:2438–2446.

McLaughlin J, Renzi D. Shear wave speed recovery in transient elastography and supersonic imaging using propagating fronts. Inverse Problems 2006;22:681–706.

Oestreicher L. Field and impedance of an oscillating shpere in a viscoelastic medium with an application to biophysics. J Acoust Soc Am 1951;23:707–714.

Pelleymounter M, Cullen M, Baker M, Hecht R, Winters D, Boone T. Effects of the obese gene product on body weight regulation in ob/ob mice. Science 1995;269:540–543.

Rouze N, Wang M, Palmeri M, Nightingale K. Robust estimation of time-of-flight shear wave speed using a radon sum transformation. IEEE Trans Ultrason Ferroelectr Freq Control 2010;57:2662–2670.

Sridhar M, Insana M. Ultrasonic measurements of breast elastography. Med Phys 2007;34:4757–4767.

Sridhar M, Liu J, Insana M. Viscoelastic imaging using ultrasound: Parameters and error analysis. Phys Med Biol 2007;52:2425–2443.

Wu Z, Hoyt K, Rubens D, Parker K. Sonoelastographic imaging of interference patterns for estimation of shear velocity distribution in biomaterials. J Acoust Soc Am 2006;120:535–545.